






RESEARCH ARTICLE | FEBRUARY 14 2024

## Control of growth kinetics during remote epitaxy of complex oxides on graphene by pulsed laser deposition

M. A. Wohlgemuth ; U. Trstenjak ; A. Sarantopoulos ; F. Gunkel ; R. Dittmann 



*APL Mater.* 12, 021113 (2024)

<https://doi.org/10.1063/5.0180001>



CrossMark



## APL Energy

## Latest Articles Online!

**Read Now**



# Control of growth kinetics during remote epitaxy of complex oxides on graphene by pulsed laser deposition

Cite as: APL Mater. 12, 021113 (2024); doi: 10.1063/5.0180001

Submitted: 6 October 2023 • Accepted: 1 January 2024 •

Published Online: 14 February 2024



M. A. Wohlgemuth,<sup>1,2,a</sup> U. Trstenjak,<sup>3</sup> A. Sarantopoulos,<sup>1,2</sup> F. Gunkel,<sup>1,2</sup> and R. Dittmann<sup>1,2</sup>

## AFFILIATIONS

<sup>1</sup>Peter Grünberg Institute 7, Forschungszentrum Jülich GmbH, 52428 Jülich, Germany

<sup>2</sup>Jülich-Aachen Research Alliance (JARA-FIT), RWTH Aachen University, 52056 Aachen, Germany

<sup>3</sup>Advanced Materials Department, Jozef Stefan Institute, 1000 Ljubljana, Slovenia

<sup>a</sup>Author to whom correspondence should be addressed: [m.wohlgemuth@fz-juelich.de](mailto:m.wohlgemuth@fz-juelich.de)

## ABSTRACT

Remote epitaxy through 2D materials opens new opportunities for research and application, overcoming some limitations of classical epitaxy and allowing the creation of freestanding layers. However, using graphene as a 2D interlayer for remote epitaxy of metal oxides is challenging, particularly when carried out by pulsed laser deposition (PLD). The graphene layer can be easily oxidized under the typically applied high oxygen pressures, and the impact of highly kinetic particles of the plasma plume can lead to severe damages. In this study, both aspects are addressed: Argon is introduced as an inert background gas in order to avoid oxidation and to reduce the kinetic impact of the plasma species on graphene. The laser spot size is minimized to control the plasma plume and particle flux. As a model system, strontium titanate (STO) is quasi-homoepitaxially grown on graphene buffered STO single crystals. Raman spectroscopy is performed to evaluate the 2D, G, and D band fingerprints of the graphene layer and to assess the defect structure of the interlayer after the deposition. Our results prove that control of the growth kinetics by reducing the laser spot size and by using high argon pressures provides a key strategy to conserve graphene with a low defect density during PLD while allowing a layer-by-layer growth of structurally coherent oxide layers. This strategy may be generalized for the PLD remote epitaxy of many complex oxides, opening the way for integrating 2D materials with complex oxides using widely accessible PLD processes.

© 2024 Author(s). All article content, except where otherwise noted, is licensed under a Creative Commons Attribution (CC BY) license (<http://creativecommons.org/licenses/by/4.0/>). <https://doi.org/10.1063/5.0180001>

## I. INTRODUCTION

Perovskite-type transition metal oxides show a large variety of electronic, magnetic, and ionotronic properties<sup>1–4</sup> and are, therefore, of high scientific interest, particularly when approaching nanoscale structures such as thin films and interfaces.<sup>5–8</sup> Here, the material's behavior can exhibit different properties from the bulk due to the confinement in one or more dimensions,<sup>9,10</sup> the bending of electronic bands,<sup>11,12</sup> and the formation of space charges.<sup>13,14</sup>

In order to achieve atomically defined crystalline thin films, oxide epitaxy via molecular beam epitaxy<sup>15</sup> and pulsed laser deposition (PLD)<sup>16</sup> have evolved as widely applied synthesis routes.

However, classical epitaxy is facing some limitations: For instance, the lattice mismatch between the substrate and the thin film, the thermodynamical instabilities of the materials, and specific growth temperatures may restrict the choice of materials. Further limitations might be undesired strain effects and interdiffusion between layers.<sup>17</sup>

To overcome these limitations, remote epitaxy through a 2D material, which serves as a buffer layer, can be used. Graphene is a commonly used material and serves as a diffusion barrier during layer deposition, preventing interfacial reactions between the substrate and the functional thin film, which can occur at high growth temperatures.<sup>18</sup> On the other hand, the graphene interlayer

still allows sufficient interactions between the substrate and the deposited film to promote a structurally coherent and epitaxial growth.<sup>19</sup>

In addition, remote epitaxy complements the so-called sacrificial layer route<sup>20–22</sup> to achieve freestanding oxide membranes. Exfoliation is possible due to the weak interlayer bondings between the graphene and the thin film, allowing for mechanical exfoliation routes. The freestanding layers can be transferred to arbitrary substrates and devices, providing new possibilities on experimental characterization and testing new functionalities.<sup>23–25</sup> Remote epitaxy through a buffering 2D layer, such as graphene, was suggested in combination with molecular beam epitaxy<sup>26</sup> and chemical vapor deposition,<sup>27</sup> as well as with PLD.<sup>28</sup> The possibility to grow complex material compositions in a stoichiometric manner and with a comparably high growth rate, which can be reached in PLD, makes it an attractive and widely used growth method for complex oxide thin films.

Nevertheless, graphene as an interlayer for PLD remote epitaxy can be quite challenging, especially for the growth of metal oxides, where a high oxygen pressure is usually required to reach the desired properties of the thin films. In addition, graphene easily reacts with oxygen, leading to oxidation and decomposition of the interlayer. Another challenge is the high kinetic impact of plasma plume particles, potentially damaging the graphene layer [cf. Figure 1(a)] and thus making PLD remote epitaxy a hardly controllable process. In this study, we overcome the challenge of the graphene layer oxidation by introducing argon as an inert background gas to the PLD system during growth. In addition, a variation of the argon growth

pressure is used to control the kinetic energy of the plasma plume particles. To further reduce the kinetic impact on our graphene buffered substrates, we minimize the laser spot size on the target, resulting in a lowered material flux and a reduced kinetic energy of the plasma plume particles.<sup>29</sup> At the same time, the laser fluence was kept constant during deposition by adjusting the laser energy to reach a comparable cation stoichiometry of the resulting thin films.<sup>30</sup> As will be demonstrated, both approaches, using argon gas and minimizing the laser spot size, are key strategies to control the growth kinetics during PLD and allow for a significant reduction in damages to the graphene layer.

To investigate the conservation of graphene interlayers under the variation of PLD parameters, we use strontium titanate (STO) as a model system. STO has a well-known defect chemistry and is a widely investigated metal oxide with a perovskite structure at room temperature, which can be quasi-homoepitaxially grown on graphene buffered STO single crystals in (001) orientation.<sup>30,31</sup> In addition, STO has a high dielectric constant,<sup>32</sup> is extensively used in resistive switching devices,<sup>33,34</sup> and can host two-dimensional electron gases,<sup>5,35</sup> making it an important model material for oxide electronic applications.

## II. EXPERIMENTAL SECTION

### A. Graphene transfer and thin film synthesis

Prior to the thin film synthesis, epi-polished (001) STO substrates (Shinkosha Co. Ltd., Japan) are etched in buffered

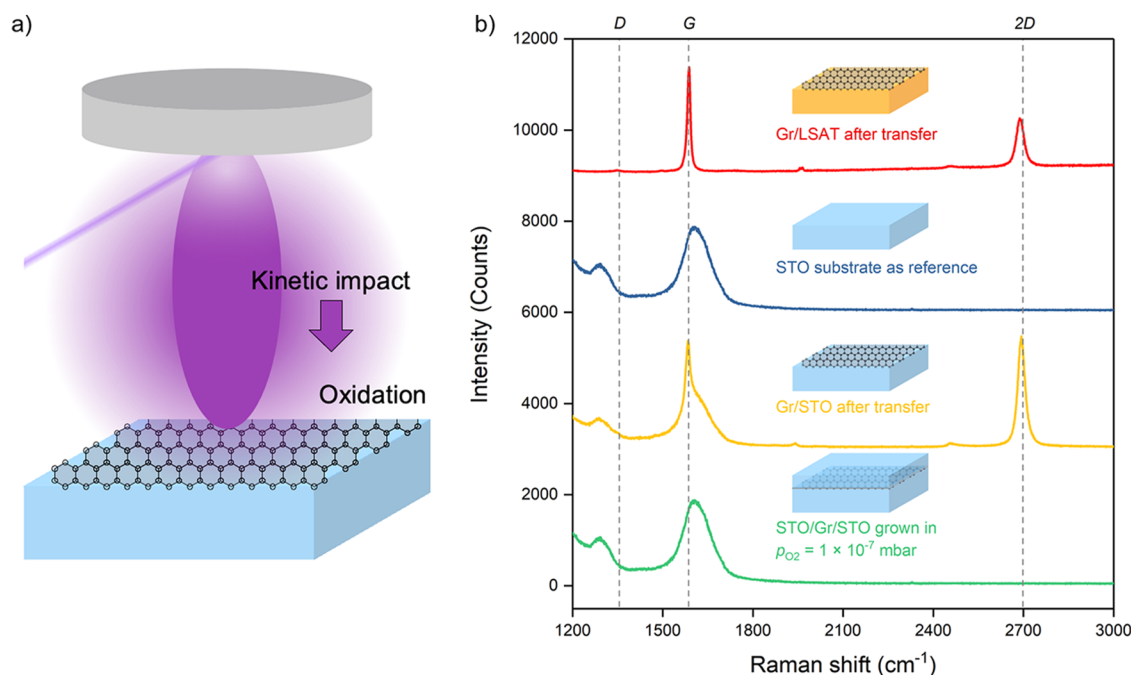


**FIG. 1.** (a) Schematic of remote epitaxy on a graphene buffered substrate using PLD. The main challenges for the conservation of the graphene layer are damages due to the kinetic impact and decomposition due to oxidation. (b) Raman spectra of graphene on LSAT after wet transfer (red), of a bare STO substrate as a reference (blue), of a graphene covered STO substrate (yellow), and of a 20 nm thick STO thin film grown on graphene buffered STO at low  $O_2$  partial pressures (green). The spectra shown are offset along the y axis for clarity.

hydrofluoric acid to achieve  $\text{TiO}_2$  termination. Subsequently, the samples are annealed at  $950^\circ\text{C}$  for 2 h in air to gain a precise step terrace structure. High-quality bilayer graphene is grown on a Cu foil via chemical vapor deposition and is coated with a polymethyl methacrylate (PMMA) layer (Graphenea, Spain). The Cu foil is dissolved in ammonium persulfate (AppliChem GmbH, Germany), and afterward, the graphene can be wet transferred to the pre-treated STO substrates. Subsequent to the wet transfer, the graphene covered sample is dried with a  $\text{N}_2$  gun and heated up to  $T = 100^\circ\text{C}$  for 10 min on a hot plate. Finally, to remove as much of the PMMA coating layer as possible, the samples are treated with acetone and isopropanol. Finally, the samples are pre-annealed at  $T = 600^\circ\text{C}$  for 2 h in the vacuum chamber of the PLD system before the deposition of the thin film.

The epitaxial STO thin films are deposited by reflection high-energy electron diffraction (RHEED)-controlled PLD (SURFACE systems + technology GmbH, Germany), operated with a KrF-excimer laser (Lambda Physik Lasertechnik, Germany) with a wavelength of  $\lambda = 248$  nm. During deposition, a laser fluence  $F = 1.05 \frac{\text{J}}{\text{cm}^2}$ , a growth temperature  $T = 830^\circ\text{C}$ , a laser frequency  $f = 5$  Hz, and a target-to-substrate distance  $d_{\text{T-S}} = 40$  mm are used (the laser spot size and background pressure are varied).

## B. Characterization of thin film and graphene interlayer

For the investigation of the surface morphology, a Cypher SPM (Research Asylum, Germany) atomic force microscope is used in tapping mode with silicon tips (NanoWorld AG, Switzerland). X-ray diffraction (XRD) and reflectivity (XRR) are performed with a D8 ADVANCE diffractometer (Bruker AXS GmbH, Germany), operated with a monochromatized  $\text{Cu K}\alpha_1$  radiation source in  $2\theta - \theta$  geometry. The spectrometer used for inductively coupled plasma-mass-spectrometry (ICP-MS) is an Agilent 7900 quadrupole mass analyzer (Agilent Technologies, USA).

For the purpose of evaluating the quality of the graphene before and after deposition, Raman spectroscopy is used to reveal the typical fingerprint peaks of graphene. These experiments are performed at room temperature using a confocal Raman microscope XploRA PLUS (Horiba, France) equipped with a 532 nm solid-state laser. The laser beam is focused in  $100\times$  magnification to a spot size of around  $0.4 \mu\text{m}$  in diameter. For the analysis of the spectra, LabSpec 6 software from Horiba is used, including signal subtraction and peak fitting. Each spectrum shown in this study is an average of five datasets measured on different spots of the sample.

## III. RESULTS AND DISCUSSION

Figure 1(b) shows a Raman spectrum obtained for a reference sample of bilayer graphene transferred on a  $(\text{La}_{0.3}\text{Sr}_{0.7})(\text{Al}_{0.65}\text{Ta}_{0.35})\text{O}_3$  (LSAT) substrate (red). One clearly observes the characteristic G band, referring to an in-plane vibrational mode of the  $\text{sp}^2$  hybridized carbon atoms of the graphene layer, appearing at around  $1590 \text{ cm}^{-1}$ , and the characteristic 2D band, referring to a two phonon lattice vibrational process, found at around  $2700 \text{ cm}^{-1}$ .<sup>36</sup>

Another important Raman fingerprint of graphene is the defect band or D band, which is activated by the presence of defects to

appear at around  $1350 \text{ cm}^{-1}$ . The D band intensity scales with the density of defects in the graphene layer. Thus, the absence of the D band signal observed for the reference sample indicates a widely intact graphene layer after the wet chemical transfer.

In contrast to the LSAT substrate, STO shows Raman activity in the same spectral range as the characteristic region of graphene. This is shown by the STO substrate reference measurement (blue), revealing the so-called R band at around  $1607 \text{ cm}^{-1}$ , as well as the Q band at around  $1292 \text{ cm}^{-1}$  and several more at lower wavenumbers,<sup>37</sup> which are outside the field of view in Fig. 1(b). When graphene is transferred onto STO, a superposition of the Raman responses of STO and graphene is observed (yellow). The absence of the D band signal and the strong appearance of G and 2D band intensities indicate the successful transfer of bilayer graphene onto STO.

Finally, the green dataset corresponds to the Raman response of a typical STO thin film deposited on a bilayer of graphene at a low oxygen pressure ( $p_{\text{O}_2} = 1 \times 10^{-7}$  mbar). In contrast to the as-transferred graphene, a complete vanishing of the graphene signal is observed in the resulting Raman spectra. This showcases the detrimental sensitivity of the graphene interlayer to the growth conditions. As a result, PLD remote epitaxy requires a careful choice and adjustment of deposition parameters departing from classical oxide PLD, in order to achieve a defined layer growth while conserving the graphene interlayer.

Since minute amounts of oxygen already result in the complete decomposition of the graphene interlayer, we adjust the PLD parameters in two steps: We first deposit STO thin films at the base pressure of the PLD system (i.e., ultra-high vacuum at  $p_{\text{UHV}} = 1 \times 10^{-8}$  mbar) to fully avoid additional oxygen supply during the process. In addition, the laser spot size is reduced, resulting in a reduced total particle flux, a lowered kinetic energy of the plume particles due to a reduced time of flight, and a reduced amount of ionized species.<sup>29</sup> Second, in the absence of oxygen gas supply, a more confined plasma plume is reached by increasing the background pressure by using argon gas during deposition. The use of argon gas allows for the growth of STO at increased absolute pressures, while keeping the oxygen partial pressure low during deposition. In addition, using a higher background pressure reduces the scattering mean free path of the plasma plume particles, lowering the kinetic impact due to enhanced scatter events during plasma propagation.

Furthermore, PLD parameters, such as growth temperature and target-to-substrate distance, are found to have no strong effect on the conservation of graphene during deposition as demonstrated by other groups, for instance by Trstenjak *et al.*<sup>38</sup>

## A. Properties of the remote-epitaxial STO thin films

### 1. Impact of laser spot size

Figure 2(a) shows the XRD and XRR data obtained for the spot size series for remote epitaxy on graphene bilayers at the base pressure. The laser spot size is varied from  $1.98 \times 1.14 \text{ mm}^2$  (corresponding to an area of  $A = 2.26 \text{ mm}^2$ ) to  $1.32 \times 1.04 \text{ mm}^2$  ( $A = 1.37 \text{ mm}^2$ ), to  $0.79 \times 0.57 \text{ mm}^2$  ( $A = 0.45 \text{ mm}^2$ ), and, finally, to  $0.48 \times 0.45 \text{ mm}^2$  ( $A = 0.22 \text{ mm}^2$ ). The total laser energy is varied accordingly to preserve a constant laser fluence of  $F = 1.05 \frac{\text{J}}{\text{cm}^2}$  for all samples, which is required for Sr:Ti cation stoichiometry deposition.<sup>30</sup>

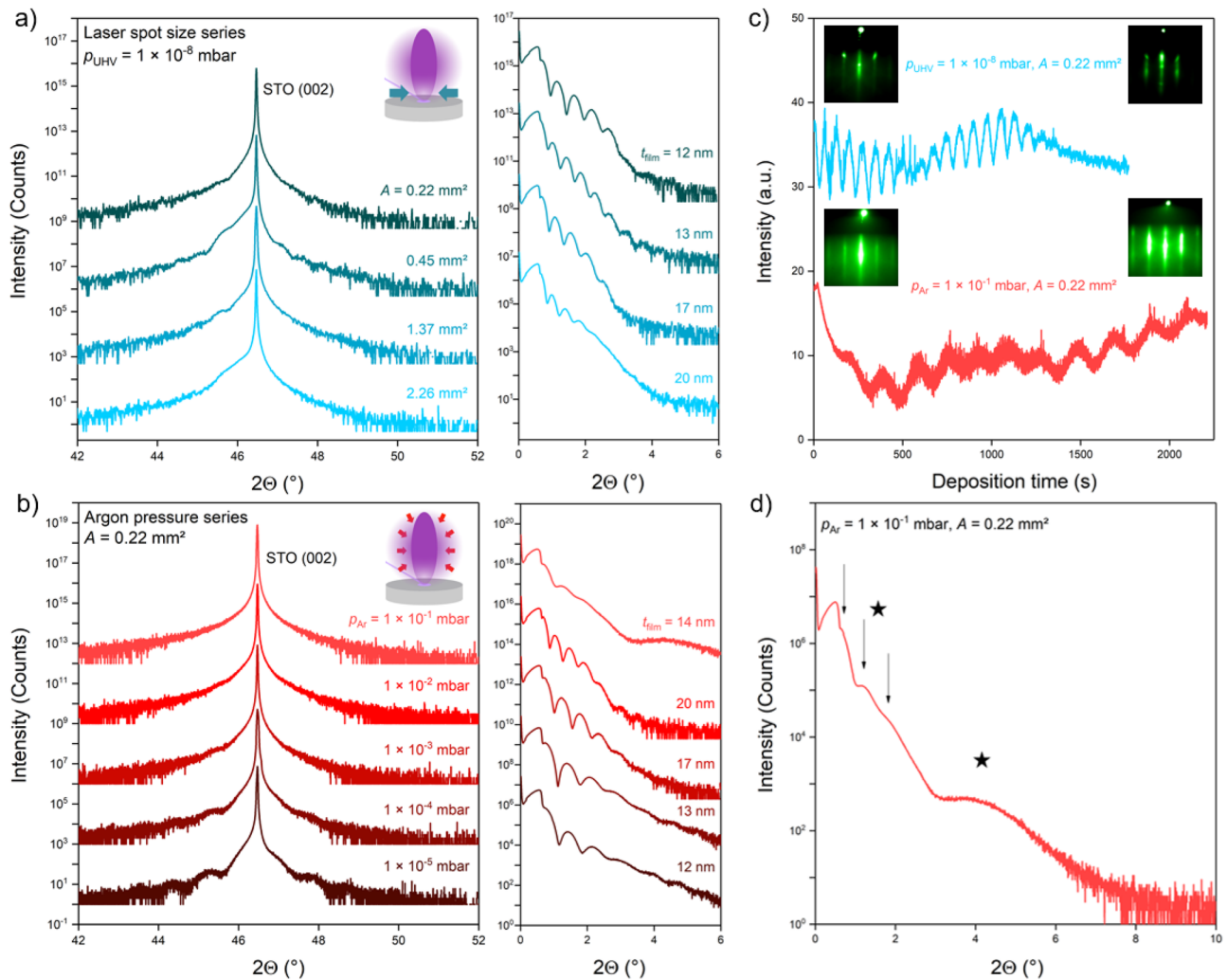


**FIG. 2.** XRD around the (002) reflection and XRR of STO thin films grown on graphene buffered STO (a) at  $p_{\text{UHV}} = 1 \times 10^{-8}$  mbar with varying laser spot sizes and (b) with a fixed laser spot size  $A = 0.22 \text{ mm}^2$  at varying argon pressures (The diffractograms/reflectograms shown are offset along the y axis for clarity). (c) RHEED oscillations and the corresponding initial and final RHEED patterns of 10 nm thick and 5 nm thick STO films grown on graphene buffered STO in UHV (top) and at  $p_{\text{Ar}} = 1 \times 10^{-1}$  mbar (bottom) with a laser spot size of  $A = 0.22 \text{ mm}^2$ . (d) XRR zoom in of the sample grown at  $p_{\text{Ar}} = 1 \times 10^{-1}$  mbar with a laser spot size of  $A = 0.22 \text{ mm}^2$ . The arrows mark the oscillations coming from a thin film layer, and the stars mark the graphene signal.

XRD is performed around the (002) reflection of the STO substrate, evident as a sharp peak at  $46.472^\circ$ . For all laser spot sizes, an additional film peak is barely distinguishable from the STO substrate peak and appears as a faint shoulder shifted to lower angles as compared to the substrate peak. Our results show that there is no significant separation between the thin film and the substrate peak, indicating successful epitaxy of the top layer and adaption of the crystal structure of the STO substrate. In particular, this result indicates the high quality of our homoepitaxy, in which the lattice constant of the film is expected to be identical to the one of the substrate. In addition, thickness oscillations are observed, indicating the presence of the deposited film. However, their intensity is faint due to the similar lattice constants as expected for a quasi-homoepitaxial

growth. Their appearance may still be preserved due to the lattice offset induced by the graphene layer<sup>39</sup> or a small offset in the lattice constant, which possibly stems from a minute residual non-stoichiometry.<sup>40,41</sup> In cases where only a weak signature of the STO layer is observed in XRD, XRR still shows well-defined oscillations, revealing the expected thin film and allowing the determination of the final film thickness, which is varying between 12 and 20 nm for different laser spot sizes.

## 2. Impact of argon pressure

Figure 2(b) shows the x-ray diffractograms and the corresponding reflectograms for samples grown at pressures between



$p_{\text{Ar}} = 1 \times 10^{-5}$  mbar and  $p_{\text{Ar}} = 1 \times 10^{-1}$  mbar. For all samples, the thin film peak is superimposed by the strong signal of the substrate, again indicating the similar lattice constants of the thin film and the substrate. Furthermore, thickness oscillations are only visible at lower pressures and, at higher pressures, the fringes vanished completely, indicating a similar cation stoichiometry of the thin film and the substrate.<sup>42</sup> However, the pronounced oscillations in XRR prove the presence of the STO layer, revealing a film thickness varying between 12 and 20 nm at different argon pressures. During deposition, RHEED is used to gain additional information about the deposition rate and the growth mode. The corresponding RHEED data during the remote epitaxy of STO are shown in Fig. 2(c). In contrast to the classical 2D-diffraction pattern with well-defined specular and diffraction spots (cf. Fig. S1 of the supplementary material), graphene covered substrates exhibit streaky patterns already in the initial stage of growth, indicating an interaction between the electrons and the graphene layer. For some parameters, both in UHV and at highest argon pressures, a layer-by-layer growth is identified by the observation of RHEED intensity oscillations, allowing the precise control of the layer thickness at the single unit cell level. For the growth in UHV, pronounced RHEED oscillations were observed (blue). In contrast, the oscillations observed for the argon series were less intense but still present (red). Compared to the growth in UHV, the deposition rate is reduced under argon atmosphere, reflected by an increased oscillation period. This is due to collisions

of the plasma plume particles with the background gas molecules, reducing their kinetic energy and the total yield of incoming plasma species during the growth. However, oscillations are not observed for all samples, preventing RHEED-guided thickness control, resulting in the thickness variation of the final samples as determined by XRR.

Next to the structural properties of the deposited STO layer, the structural characterization of the samples contains additional signatures, which we assign to the presence of the graphene interlayers. Revisiting the XRR data of the high argon pressure sample, Fig. 2(d) reveals a second oscillation period (highlighted by the stars), which is much broader than the relatively narrow oscillations, detectable for all samples and related to the STO film (highlighted by the arrows). This second oscillation is reproducibly observed for samples grown at  $p_{\text{Ar}} = 1 \times 10^{-1}$  mbar and  $A = 0.22 \text{ mm}^2$ . This additional periodicity may be attributed to the graphene layer, revealing an estimated interlayer thickness of  $d = 2.8 \text{ nm}$ . This value is greater than expected for a bilayer of graphene<sup>43</sup> but corresponds to a similar periodicity as observed for a nominal graphene layer as transferred to the STO substrate (cf. Fig. S2 of the supplementary material). A similar observation was reported in the literature and attributed to the wrinkling and folding of the graphene layer during the wet-chemical transfer.<sup>26</sup> Additionally, increased graphene layer thicknesses were reported as a result of chemical modifications,<sup>44</sup> impurities, and point defects,<sup>45</sup> which may still be induced during

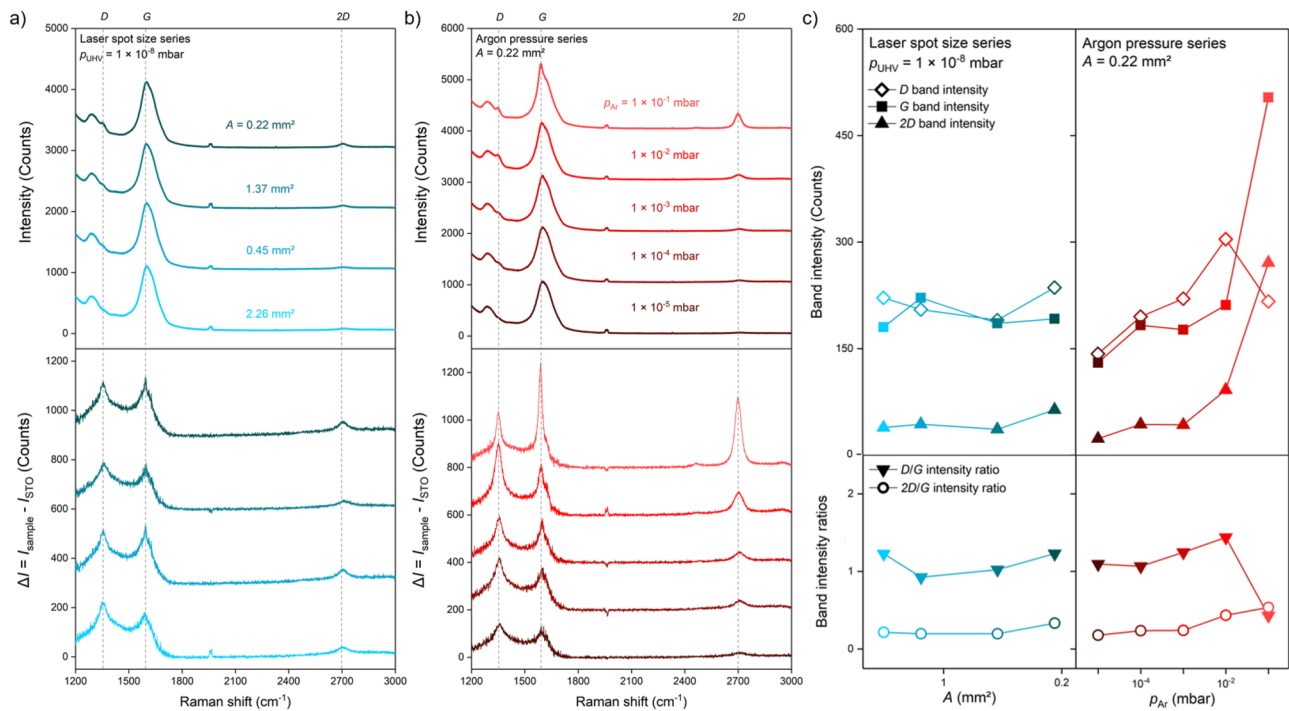


**FIG. 3.** Raman spectra of STO thin films grown on graphene buffered STO (a) at  $p_{\text{UHV}} = 1 \times 10^{-8}$  mbar with varying laser spot sizes and (b) with a fixed laser spot size  $A = 0.22 \text{ mm}^2$  at varying argon pressures. The top plot displays the uncorrected data, and the bottom plot shows the same Raman spectra after normalization and subtraction of the STO signal (The spectra shown are offset along the y axis for clarity). (c) Corrected band intensities of Raman signals of STO thin films grown on graphene buffered STO at  $p_{\text{UHV}} = 1 \times 10^{-8}$  mbar with varying laser spot sizes (left) and with a fixed laser spot size  $A = 0.22 \text{ mm}^2$  (right) at varying argon pressures.

the transfer process. Yet, the appearance of this additional periodicity may indicate that the graphene layer is widely conserved during growth at high argon pressures.

Summarizing these results, we find that all samples have similar crystallographic properties. Occasionally, even RHEED intensity oscillations are observed, indicative of a layer-by-layer growth mode during remote epitaxy. Furthermore, a comparable surface morphology is proven by atomic force microscopy (AFM; cf. Fig. S3 of the supplementary material). For all samples, we find a similar cation stoichiometry close to stoichiometric compositions, as inferred from negligible peak shifts in XRD. This result was further corroborated from the ICP-MS data obtained from reference samples grown on NdGaO<sub>3</sub> (NGO) under the same conditions (cf. Fig. S4 of the supplementary material).

## B. Raman analysis of the graphene interlayer

### 1. Impact of laser spot size

In order to investigate the graphene interlayers after deposition, Raman spectroscopy is applied to all samples. In Fig. 3(a), the results for the samples grown in UHV with different laser spot sizes are shown. For all laser spot sizes, only faint signatures of the Raman fingerprints of graphene are evident. In particular, the G band is barely distinguishable from the STO resonance at around 1607 cm<sup>-1</sup>. However, the 2D band shows a slight increase in intensity with a reduced laser spot size and a particle flux. In the spectral region of the D band, weak Raman responses are observed.

In order to evaluate the spectra more quantitatively, all spectra are normalized with respect to the STO G band at around 307 cm<sup>-1</sup> (this resonance is outside the field of view in Fig. 3 but is illustrated in detail in Fig. S5 of the supplementary material). Subsequently, the spectra are corrected by subtracting the STO reference signal (cf. Fig. S6 of supplementary material). The resulting intensity difference,  $\Delta I = I_{\text{sample}} - I_{\text{STO}}$ , is plotted in the bottom panel of Fig. 3(a), confirming the presence of 2D, G, and D bands of graphene in the spectra. It becomes evident that for all laser spot sizes, a graphene layer is, indeed, conserved. Despite the low intensity and similar D band and G band intensities, the rise in the 2D band indicates that a smaller laser spot size and thus growth at a lower total particle flux is preferable.

### 2. Impact of argon pressure

Figure 3(b) shows the Raman spectra obtained for the samples grown at different argon pressures. Here, a much clearer trend is observed: With an increase in the argon pressure, 2D and G peak intensities increase significantly. This trend is most evident in the substrate-corrected difference spectra (bottom panel), showing a much higher intensity of the graphene fingerprints at high argon pressures than that observed for all samples grown in UHV and at lower argon pressures. Likewise, the D band intensity increases with increasing intensities of the 2D and G bands, exhibiting a comparable or even larger intensity than the G band in the pressure range  $p_{\text{Ar}} = 1 \times 10^{-5}$  mbar to  $p_{\text{Ar}} = 1 \times 10^{-2}$  mbar. Only for the highest applied argon pressure of  $p_{\text{Ar}} = 1 \times 10^{-1}$  mbar, the intensity of the G band strongly exceeds the intensity of the D band.

In the top panel of Fig. 3(c), the 2D and G band peak intensities and the D band intensity are summarized, for both the laser spot size and the argon pressure series, highlighting the strong intensity

increase for samples grown at highest argon pressures, exceeding the intensity of all samples grown under ballistic growth conditions in UHV. For the argon pressure series, we observe that the 2D and G band intensities increase with an increase in pressure, reaching a significantly enhanced intensity at the highest argon pressure applied. Notably, the D band intensity drops when grown at highest argon pressures, indicating that less defects are present in graphene under these conditions.

The intensity ratios of the 2D and G bands and those of the D and G bands are given in the bottom panel of Fig. 3(c). This allows a more detailed assessment of the graphene interlayer and its defect concentration based on the three-stage model for disordered and amorphous carbon.<sup>46</sup> The  $I_{2D}/I_G$  ratios determined for all samples of the laser spot series are similar and below 0.5. In principle, this ratio can be used to determine the number of graphene layers. The low value measured here might indicate that a multilayer of graphene is present. Instead, we assume that a high defect concentration, possibly coming from charged impurities, leads to this low ratio.<sup>47</sup> However, the overall intensity of the graphene fingerprints under these conditions is low, and the same applies to the samples grown in the pressure range  $p_{\text{Ar}} = 1 \times 10^{-5}$  mbar to  $p_{\text{Ar}} = 1 \times 10^{-3}$  mbar. With higher argon pressures, the ratio approaches and finally exceeds 0.5 for samples grown at  $p_{\text{Ar}} = 1 \times 10^{-1}$  mbar, indicative of a lowered defect concentration inside the graphene interlayer.

For the  $I_D/I_G$  ratio, the values determined for the laser spot series are similar, indicating that the variation in this PLD parameter has a smaller impact on conserving the graphene layer during deposition. Comparing the  $I_D/I_G$  ratios of the laser spot size series and the argon pressure series, we find that they are in the same range. However, for the sample grown at highest argon pressures, it drops dramatically compared to all other samples, indicating that the relative defect concentration in the graphene interlayer is significantly reduced under these conditions. This is consistent with the observed  $\Delta I$  of all graphene fingerprints in this sample.

Hence, our results indicate that using argon as a background gas is most effective in conserving the graphene interlayer during deposition. This is because argon gas results in a reduced kinetic energy of the plasma plume particles, due to collisions of the particles with the ambient gas. In this way, a quasi-thermalized growth is achieved, while keeping the oxygen pressure low enough to avoid complete oxidation and decomposition of the graphene layer.

## IV. CONCLUSION

We demonstrate the successful synthesis of crystalline STO thin films on graphene buffered STO substrates by remote epitaxy using PLD. While these optimized growth conditions depart from the typical growth conditions for complex oxides in PLD, we still obtain well-defined and structurally coherent homoepitaxial thin films close to stoichiometric composition. We prove that the conservation of the graphene interlayer is possible by the control of the growth kinetics during deposition. The kinetic impact of the plasma species can be controlled by reducing the laser spot size, decreasing the total flux of incoming particles, and especially by increasing the argon pressure, lowering the kinetic energy of the particles while avoiding oxidation. At an argon pressure  $p_{\text{Ar}} = 1 \times 10^{-1}$  mbar combined with a laser spot size  $A = 0.22$  mm<sup>2</sup>,

the best results are achieved in terms of graphene conservation, which is indicated by the appearance of clear XRR thickness oscillations owing to the graphene layer, the significantly enhanced intensities of the graphene fingerprints in Raman analysis, and the reduced relative intensity of the *D* band. The RHEED data even show that a layer-by-layer growth mode is possible under these conditions.

Our systematic study reveals that the combination of a reduced laser spot size and an increased inert gas pressure are key to avoid severe damages to the graphene layer during PLD remote epitaxy. This strategy may be generalized for many other complex oxides as the individual control of oxidation processes and of the kinetic impact during growth is possible. In addition, it may also be adopted in a heteroepitaxy approach to combine different complex oxides. The resulting graphene/metal oxide bilayers may, for instance, be employed as functional units harvesting the graphene layer as a bottom electrode to address the oxide layer. Moreover, magnetic or ferroelectric oxides may be used to control the properties of the graphene layer via proximity phenomena, which could give rise to new phenomena and device structures. Finally, the conservation of the graphene layers under the PLD process reflects the first step toward mechanical exfoliation of freestanding oxides, which requires intact graphene interlayers as a crucial prerequisite. The PLD remote epitaxy approach then allows us to access the various degrees of freedom of epitaxial systems, including heterostructuring and controlled crystal orientations of graphene/metal oxide bilayers. Moreover, a similar strategy may be employed when using alternative 2D buffer materials, such as h-BN, WS<sub>2</sub>, and MoS<sub>2</sub>, in the remote epitaxy approach, as these possess similar challenges of strong oxidation and defect sensitivity as graphene.<sup>48,49</sup> Hence, the control of the kinetic impact during PLD can be a successful route to implement remote epitaxy of complex oxides at an improved layer and interlayer quality, opening the way for the exploration of new device concepts and material combinations.

## SUPPLEMENTARY MATERIAL

Additional data and characterizations relevant to this article, which are referred to in the main text, including Figs. S1–S6, are provided in the supplementary material.

## ACKNOWLEDGMENTS

We sincerely thank Zhaodong Wang and Kalle Goß for fruitful discussions and thank René Borowski, Grigory Potemkin, and Thorsten Brazda for the technical support. We thank Astrid Küppers for ICP-MS measurements. This research was financially supported by FLAG-ERA JTC 2019 project Transferable two-dimensional correlated oxide layers (To2Dox) through Deutsche Forschungsgemeinschaft (DFG, Project No. 436610738/DI 919/8-1). A.S. acknowledges the funding provided by the BMBF project NEUROTEC (Project Nos. 16ME0398K and 16ME0399).

## AUTHOR DECLARATIONS

### Conflict of Interest

The authors have no conflicts to disclose.

## Author Contributions

**M. A. Wohlgenuth:** Conceptualization (equal); Data curation (equal); Formal analysis (equal); Funding acquisition (equal); Investigation (equal); Methodology (equal); Project administration (equal); Resources (equal); Supervision (equal); Validation (equal); Visualization (equal); Writing – original draft (equal); Writing – review & editing (equal). **U. Trstenjak:** Conceptualization (equal); Data curation (equal); Formal analysis (equal); Supervision (equal); Validation (equal); Writing – review & editing (equal). **A. Sarantopoulos:** Data curation (equal); Formal analysis (equal); Writing – review & editing (equal). **F. Gunkel:** Conceptualization (equal); Data curation (equal); Formal analysis (equal); Funding acquisition (equal); Project administration (equal); Resources (equal); Software (equal); Supervision (equal); Validation (equal); Visualization (equal); Writing – review & editing (equal). **R. Dittmann:** Conceptualization (equal); Data curation (equal); Formal analysis (equal); Funding acquisition (equal); Investigation (equal); Project administration (equal); Software (equal); Supervision (equal); Validation (equal); Writing – review & editing (equal).

## DATA AVAILABILITY

The data that support the findings of this study are available within the article and its supplementary material.

## REFERENCES

- R. Dittmann, S. Menzel, and R. Waser, “Nanoionic memristive phenomena in metal oxides: The valence change mechanism,” *Adv. Phys.* **70**, 155 (2021).
- D. G. Schlom, J. Mannhart *et al.*, “Interface takes charge over Si,” *Nat. Mater.* **10**, 168 (2011).
- F. Gunkel, D. V. Christensen, Y. Z. Chen, and N. Pryds, “Oxygen vacancies: The (in)visible friend of oxide electronics,” *Appl. Phys. Lett.* **116**, 120505 (2020).
- H. Y. Hwang, Y. Iwasa, M. Kawasaki, B. Keimer, N. Nagaosa, and Y. Tokura, “Emergent phenomena at oxide interfaces,” *Nat. Mater.* **11**, 103 (2012).
- A. Ohtomo and H. Y. Hwang, “A high-mobility electron gas at the LaAlO<sub>3</sub>/SrTiO<sub>3</sub> heterointerface,” *Nature* **427**, 423 (2004).
- J. Mannhart and D. G. Schlom, “Oxide interfaces—An opportunity for electronics,” *Science* **327**, 1607 (2010).
- M.-A. Rose, B. Smid, M. Vorokhta, I. Slipukhina, M. Andrä, H. Bluhm, T. Duchon, M. Lezaic, S. A. Chambers, R. Dittmann, D. N. Mueller, and F. Gunkel, “Identifying ionic and electronic charge transfer at oxide heterointerfaces,” *Adv. Mater.* **33**, e2004132 (2021).
- H. Yan *et al.*, “Stoichiometry and termination control of LaAlO<sub>3</sub>/SrTiO<sub>3</sub> bilayer interfaces,” *Adv. Mater. Interfaces* **8**, 2001477 (2021).
- G. Cheng, P. F. Siles, F. Bi, C. Cen, D. F. Bogorin, C. W. Bark, C. M. Folkman, J.-W. Park, C.-B. Eom, G. Medeiros-Ribeiro, and J. Levy, “Sketched oxide single-electron transistor,” *Nat. Nanotechnol.* **6**, 343 (2011).
- T. Nguyen, V. H. Hoang, T.-Y. Koo, N.-S. Lee, and H.-J. Kim, “Modulation of metal-insulator transitions of NdNiO<sub>3</sub>/LaNiO<sub>3</sub>/NdNiO<sub>3</sub> trilayers via thickness control of the LaNiO<sub>3</sub> layer,” *Sci. Rep.* **9**, 20145 (2019).
- Y. Z. Chen, J. L. Zhao, J. R. Sun, N. Pryds, and B. G. Shen, “Resistance switching at the interface of LaAlO<sub>3</sub>/SrTiO<sub>3</sub>,” *Appl. Phys. Lett.* **97**, 123102 (2010).
- M. L. Reinle-Schmitt, C. Cancellieri, D. Li, D. Fontaine, M. Medarde, E. Pomjakushina, C. W. Schneider, S. Gariglio, P. H. Ghosez, J.-M. Triscone, and P. R. Willmott, “Tunable conductivity threshold at polar oxide interfaces,” *Nat. Commun.* **3**, 932 (2012).
- T. Defferriere, D. Klotz, J. C. Gonzalez-Rosillo, J. L. M. Rupp, and H. L. Tuller, “Photo-enhanced ionic conductivity across grain boundaries in polycrystalline ceramics,” *Nat. Mater.* **21**, 438 (2022).



- <sup>14</sup>R. A. De Souza, F. Gunkel, S. Hoffmann-Eifert, and R. Dittmann, "Finite-size versus interface-proximity effects in thin-film epitaxial SrTiO<sub>3</sub>," *Phys. Rev. B* **89**, 241401 (2014).
- <sup>15</sup>B. Jalan, P. Moetaf, and S. Stemmer, "Molecular beam epitaxy of SrTiO<sub>3</sub> with a growth window," *Appl. Phys. Lett.* **95**, 032906 (2009).
- <sup>16</sup>R. Dittmann and A. Sambri, *Stoichiometry in Epitaxial Oxide Thin Films in Epitaxial Growth of Complex Metal Oxides*, 2nd ed. (Woodhead Publishing, 2022).
- <sup>17</sup>M. Boota, E. P. Houwman, M. D. Nguyen, G. Lanzara, and G. Rijnders, "Effect of fabrication conditions on phase formation and properties of epitaxial (PbMg<sub>1/3</sub>Nb<sub>2/3</sub>O<sub>3</sub>)<sub>0.67</sub>-(PbTiO<sub>3</sub>)<sub>0.33</sub> thin films on (001) SrTiO<sub>3</sub>," *Am. Inst. Phys. Adv.* **6**, 055303 (2016).
- <sup>18</sup>S. A. Lee, J.-Y. Hwang, E. S. Kim, S. W. Kim, and W. S. Choi, "Highly oriented SrTiO<sub>3</sub> thin film on graphene substrate," *ACS Appl. Mater. Interfaces* **9**, 3246 (2017).
- <sup>19</sup>Z. Liu, B. Liu, Z. Chen, S. Yang, Z. Liu, T. Wei, P. Gao, and Z. Liu, "Two-dimensional material-assisted remote epitaxy and van der Waals epitaxy: A review," *Nat. Sci. Open* **2**, 20220068 (2023).
- <sup>20</sup>D. Lu, D. J. Baek, S. S. Hong, L. F. Kourkoutis, Y. Hikita, and H. Y. Hwang, "Synthesis of freestanding single-crystal perovskite films and heterostructures by etching of sacrificial water-soluble layers," *Nat. Mater.* **15**, 1255 (2016).
- <sup>21</sup>S. Puebla, T. Pucher, V. Rouco, G. Sanchez-Santolino, Y. Xie, V. Zamora, F. A. Cuellar, F. J. Mompean, C. Leon, J. O. Island, M. Garcia-Hernandez, J. Santamaria, C. Munuera, and A. Castellanos-Gomez, "Combining freestanding ferroelectric perovskite oxides with two-dimensional semiconductors for high performance transistors," *Nano Lett.* **22**, 7457 (2022).
- <sup>22</sup>Y.-W. Chang, P.-C. Wu, J.-B. Yi, Y.-C. Liu, Y. Chou, Y.-C. Chou, and J.-C. Yang, "A fast route towards freestanding single-crystalline oxide thin films by using YBa<sub>2</sub>Cu<sub>3</sub>O<sub>7-x</sub> as a sacrificial layer," *Nanoscale Res. Lett.* **15**, 172 (2020).
- <sup>23</sup>Y. Li, C. Xiang, F. M. Chiabrera, S. Yun, H. Zhang, D. J. Kelly, R. T. Dahm, C. K. R. Kierchert, T. E. L. Cozannet, F. Trier, D. V. Christensen, T. J. Booth, S. B. Simonsen, S. Kadhodazadeh, T. S. Jespersen, and N. Pryds, "Stacking and twisting of freestanding complex oxide thin films," *Adv. Mater.* **34**, e2203187 (2022).
- <sup>24</sup>R. Xu, J. Huang, E. S. Barnard, S. S. Hong, P. Singh, E. K. Wong, T. Jansen, V. Harbola, J. Xiao, B. Y. Wang, S. Crossley, D. Lu, S. Liu, and H. Y. Hwang, "Strain-induced room-temperature ferroelectricity in SrTiO<sub>3</sub> membranes," *Nat. Commun.* **11**, 3141 (2020).
- <sup>25</sup>D. Pesquera, E. Parsonnet, A. Qualls, R. Xu, A. J. Gubser, J. Kim, Y. Jiang, G. Valde, Y.-L. Huang, H. Y. Hwang, R. Ramesh, and L. W. Martin, "Beyond substrates: Strain engineering of ferroelectric membranes," *Adv. Mater.* **32**, 2003780 (2020).
- <sup>26</sup>H. Yoon, T. K. Truttmann, F. Liu, B. E. Matthews, S. Choo, Q. Su, V. Saraswat, S. Manzo, M. S. Arnold, M. E. Bowden, J. K. Kawasaki, S. J. Koester, S. R. Spurgeon, S. A. Chambers, and B. Jalan, "Free-standing epitaxial SrTiO<sub>3</sub> nanomembranes via remote epitaxy using hybrid molecular beam epitaxy," *Sci. Adv.* **8**, eadd5328 (2022).
- <sup>27</sup>Y. Kim, S. S. Cruz, K. Lee, B. O. Alawode, C. Choi, Y. Song, J. M. Johnson, C. Heidelberger, W. Kong, S. Choi, K. Qiao, I. Almansouri, E. A. Fitzgerald, J. Kong, A. M. Kolpak, J. Hwang, and J. Kim, "Remote epitaxy through graphene enables two-dimensional material-based layer transfer," *Nature* **544**, 340 (2017).
- <sup>28</sup>H. S. Kum, H. Lee, S. Kim, S. Lindemann, W. Kong, K. Qiao, P. Chen, J. Irwin, J. H. Lee, S. Xie, S. Subramanian, J. Shim, S.-H. Bae, C. Choi, L. Ranno, S. Seo, S. Lee, J. Bauer, H. Li, K. Lee, J. A. Robinson, C. A. Ross, D. G. Schlom, M. S. Rzechowski, C.-B. Eom, and J. Kim, "Heterogeneous integration of single-crystalline complex-oxide membranes," *Nature* **578**, 75 (2020).
- <sup>29</sup>H. N. Lee, S. S. Ambrose Seo, W. S. Choi, and C. M. Rouleau, "Growth control of oxygen stoichiometry in homoepitaxial SrTiO<sub>3</sub> films by pulsed laser epitaxy in high vacuum," *Sci. Rep.* **6**, 19941 (2016).
- <sup>30</sup>S. Wicklein, A. Sambri, S. Amoruso, X. Wang, R. Bruzzese, A. Koehl, and R. Dittmann, "Pulsed laser ablation of complex oxides: The role of congruent ablation and preferential scattering for the film stoichiometry," *Appl. Phys. Lett.* **101**, 13160 (2012).
- <sup>31</sup>R. Groenen, J. Smit, K. Orsel, A. Vailionis, B. Bastiaens, M. Huijben, K. Boller, G. Rijnders, and G. Koster, "Research update: Stoichiometry controlled oxide thin film growth by pulsed laser deposition," *APL Mater.* **3**, 070701 (2015).
- <sup>32</sup>W. Martienssen and H. Warlimont, *Springer Handbook of Condensed Matter and Materials Data* (Springer, 2005).
- <sup>33</sup>K. Szot, R. Dittmann, W. Speier, and R. Waser, "Nanoscale resistive switching in SrTiO<sub>3</sub> thin film," *Phys. Status Solidi RRL* **1**, R86 (2007).
- <sup>34</sup>R. Waser, R. Dittmann, G. Staikov, and K. Szot, "Redox-based resistive switching memories – Nanoionic mechanisms, prospects, and challenges," *Adv. Mater.* **21**, 2632 (2009).
- <sup>35</sup>A. F. Santander-Syro, O. Copie, T. Kondo, F. Fortuna, S. Pailhès, R. Weht, X. G. Qiu, F. Bertran, A. Nicolaou, A. Taleb-Ibrahimi, P. Le Fèvre, G. Herranz, M. Bibes, N. Reyren, Y. Apertet, P. Lecoeur, A. Barthélémy, and M. J. Rozenberg, "Two-dimensional electron gas with universal subbands at the surface of SrTiO<sub>3</sub>," *Nature* **469**, 189 (2011).
- <sup>36</sup>A. C. Ferrari, J. C. Meyer, V. Scardaci, C. Casiraghi, M. Lazzeri, F. Mauri, S. Piscanec, D. Jiang, K. S. Novoselov, S. Roth, and A. K. Geim, "Raman spectrum of graphene and graphene layers," *Phys. Rev. Lett.* **97**, 187401 (2006).
- <sup>37</sup>U. Balachandran and N. G. Eror, "Raman spectra of strontium titanate," *J. Am. Ceram. Soc.* **65**, c54 (1982).
- <sup>38</sup>U. Trstenjak, K. Goß, A. Gutsche, J. Jo, M. Wohlgemuth, R. E. Dunin-Borkowski, F. Gunkel, and R. Dittmann, "Heterogeneous integration of graphene and HfO<sub>2</sub> memristors," *Adv. Funct. Mater.* (published online) (2024).
- <sup>39</sup>J. Lee, P. Jadhav, and M. A. Baldo, "High efficiency organic multilayer photodetectors based on singlet exciton fission," *Appl. Phys. Lett.* **95**, 033301 (2009).
- <sup>40</sup>T. Ohnishi, M. Lippmaa, T. Yamamoto, S. Meguro, and H. Koinuma, "Improved stoichiometry and misfit control in perovskite thin film formation at a critical fluence by pulsed laser deposition," *Appl. Phys. Lett.* **87**, 241919 (2005).
- <sup>41</sup>D. J. Keeble, S. Wicklein, L. Jin, C. L. Jia, W. Egger, and R. Dittmann, "Nonstoichiometry accommodation in SrTiO<sub>3</sub> thin films studied by positron annihilation and electron microscopy," *Phys. Rev. B* **87**, 195409 (2013).
- <sup>42</sup>C. Xu, S. Wicklein, A. Sambri, S. Amoruso, M. Moors, and R. Dittmann, "Impact of the interplay between nonstoichiometry and kinetic energy of the plume species on the growth mode of SrTiO<sub>3</sub> thin films," *J. Phys. D: Appl. Phys.* **47**, 034009 (2014).
- <sup>43</sup>G. E. Bacon, "The interlayer spacing of graphite," *Acta Crystallogr.* **4**, 558 (1951).
- <sup>44</sup>P. Solís-Fernández, J. I. Paredes, S. Villar-Rodil, A. Martínez-Alonso, and J. M. D. Tascón, "Determining the thickness of chemically modified graphenes by scanning probe microscopy," *Carbon* **48**, 2657 (2010).
- <sup>45</sup>B. Zou, C. Walker, K. Wang, V. Tileli, O. Shafarost, N. M. Harrison, N. Klein, N. M. Alford, and P. K. Petrov, "Growth of epitaxial oxide thin films on graphene," *Sci. Rep.* **6**, 31511 (2016).
- <sup>46</sup>A. C. Ferrari and J. Robertson, "Interpretation of Raman spectra of disordered and amorphous carbon," *Phys. Rev. B* **61**, 14095 (2000).
- <sup>47</sup>C. Casiraghi, S. Pisana, K. S. Novoselov, A. K. Geim, and A. C. Ferrari, "Raman fingerprint of charged impurities in graphene," *Appl. Phys. Lett.* **91**, 233108 (2007).
- <sup>48</sup>H. Nan, Z. Wang, W. Wang, Z. Liang, Y. Lu, Q. Chen, D. He, P. Tan, F. Miao, X. Wang, J. Wang, and Z. Ni, "Strong photoluminescence enhancement of MoS<sub>2</sub> through defect engineering and oxygen bonding," *ACS Nano* **8**, 5738 (2014).
- <sup>49</sup>E. H. Åhlgren, A. Markevich, S. Scharinger, B. Fickl, G. Zagler, F. Herterich, N. McEvoy, C. Mangler, and J. Kotakoski, "Atomic-scale oxygen-mediated etching of 2D MoS<sub>2</sub> and MoTe<sub>2</sub>," *Adv. Mater. Interfaces* **9**, 2200987 (2022).